A Low-Cost Electrowetting on Dielectric Semi-Continuous Pump for Application to Microfluidic Reconfigurable Devices

David Parsi[1], Josh Augenstein[1], R. Daniel Maynes[1], Nathan B. Crane[1]

[1]*Department of Mechanical Engineering, Brigham Young University, 350 Engineering Building, Provo, UT 84602, USA.*

ABSTRACT

An electrowetting on dielectric (EWOD) pump is a microfluidic pump that uses electrowetting to manipulate liquid droplets in a chanel, offering an alternative approach to traditional mechanical pumps. EWOD-based pumps have significant potential for various microfluidic applications. For instance, by integrating microfluidic pumps with a radio frequency (RF) device, it is possible to create a microfluidic reconfigurable RF device. However, the current microfluidic-based devices have been primarily designed based on mechanical micropumps which require expensive clean-room fabrication methods. Here, we present an analytical model for an EWOD semi-continuous pump that can offer a promising alternative actuation for microfluidic actuation.However, a literature survey of recent advances in EWOD pumping has highlighted a gap in the modeling of the relationship between the fluid mechanics and the actuation dynamics. This paper presents an analytical model of an EWOD pump that determines the flow rate and pressure generated by taking into account the competing electrowetting force, friction force, and fluid inertia force in a one-degree-of-freedom channel. The analytical model is valuable for designing and optimizing EWOD-based pumps, as it provides insights into the dominant physical processes and could enable better control. The model is validated with an EWOD experiment and the data demonstrates less than a 6% error between the measured and predicted maximum droplet velocity and a maximum 7.4% error in the EWOD pump static pressure.

Keywords: Electrowetting on dielectric; Microfluidic reconfigurable radio frequency; Micropump; Semi-Continuous Pump.

1. Introduction

The concept of microfluidics was introduced over fifty years ago to miniaturize and integrate electronic and fluidic components for faster and more efficient performance [1]. Following the initial development of microfluidics, Narayanamurthy et al. published a seminal review paper about micro-pumping technologies and different actuating principles [2], including electrokinetic, pneumatic, and mechanical means [2].However, it did not address the electrowetting on dielectric (EWOD) pumping technique. An EWOD pump uses electric fields to manipulate droplets of fluid on a surface. EWOD is a phenomenon where the apparent contact angle of a liquid droplet on a dielectric surface is manipulated by applying an electric field between the droplet and the surface. By energizing individual electrodes, the droplet can be moved or manipulated in a controlled manner [3].

By applying electrical field around the contact line, the droplet will spread. The relationship between the zero-potential contact angle (θ_0), and the apparent contact angle under applied potential (θ_{EW}), and the applied voltage (V) is described by the Young/Lippmann equation [4]:

$$\cos(\theta_{EW}) - \cos(\theta_0) = \frac{\varepsilon_0 \varepsilon_r V^2}{2\gamma_{LG} d} \quad (1)$$

where ε_0 is the dielectric constant of ambient, ε_r is the dielectric constant of liquid, d is the dielectric thickness, and γ_{LG} is the surface tension of the liquid-ambient interface. By applying voltage, the contact angle will decrease until it reaches a saturation limit, which means that an additional voltage will not reduce the contact angle any further [5]. Both DC and AC signals may be used for actuation [6].

Many possible configurations can be implemented in EWOD (Figure 1), such as a grounded-droplet, floating-droplet, and diode-based configurations [7], [8]. Each has a different response to the applied voltages. The most common configuration is the grounded droplet [9]. In the grounded configuration, the droplet spreads over the energized electrodes until the droplet/electrode overlap is maximized. In the floating configuration, when the potential is applied to one of the electrodes, the droplet covers equal area of both electrodes, while in the diode configuration, the droplet moves toward the positive voltage [7].

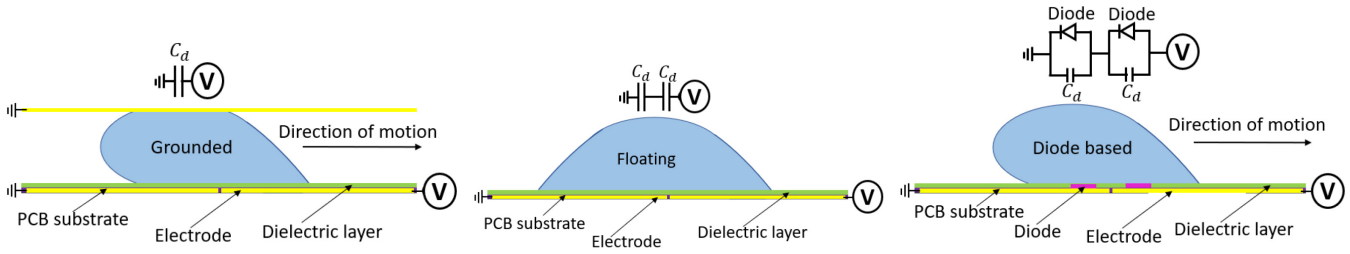

(a) (b) (c)

Figure 1. Possible configurations of an EWOD system: a) Grounded droplet with no top plate (one capacitor), in this configuration, the droplet moves to the active electrodes until the droplet is entirely on top of the active electrode b) Floating droplet (two capacitors connected in series) in this configuration, the droplet covers equal area of both electrodes, c) Diode-based continuous electrowetting (two diodes and two capacitors. One diode is connected in parallel with one capacitor and another identical pair is then connected to it back-to-back) in this configuration, the droplet moves toward the positive voltage. In all figures, Cd is the capacitance of the dielectric.

EWOD systems offer diverse applications in electronic cooling [10], optical displays [11], micro viscometers [12], micro conveyor systems [13], particle sampling and separation [14], and microbubble manipulation [15]. However, the most prominent use of EWOD technology lies in biochemical medical research, where its versatility has revolutionized the development of lab-on-chip (LOC) technology [16]. The ability to rapidly transport droplets and seamlessly integrate sensors has positioned EWOD-based microfluidic technology as a valuable tool in on-chip droplet creation and distribution.

Previous research has advanced the use of EWOD for pumps and pumping components. there is a growing interest in utilizing EWOD systems as pumps, expanding the potential applications of this technology.

Morishita et al. developed a three-face EWOD device that increases the driving force by driving a droplet from both the bottom and sides. This breakthrough allowed for the simultaneous integration of EWOD digital and channel-based microfluidics, opening up new possibilities for complex fluid manipulation and control [17]. [17]Yang and Liu demonstrated both theoretically and experimentally that an EWOD device could be used to create an air valve [18]. This valve system effectively mitigates problems commonly associated with mechanical valve systems, such as performance decay and backflow. Another recent study was conducted by Phi et al. in 2021 on EWOD-driven micropumps. They fabricated EWOD micro pump devices at the wafer level by combining EWOD with Texla valves to create a pump without moving parts [19]. By doing so, they were able to achieve flow rates of up to 100 μL/s through their device. Their study underscores the potential of combining EWOD technology with other microfluidic components to create innovative solutions for fluid manipulation and control.

Kedzierski et al. showed that their EWOD pump could be used as a semicontinuous pump for oil or water, droplet generators, and pressure regulators. This can be useful in situations where a precise and controlled amount of fluid is needed at specific intervals. EWOD pumps can be programmed to provide accurate droplet volumes and frequencies, making them well-suited for semicontinuous pumping applications [20]. Other work has been done to develop a micropump based on oscillating continuous electrowetting actuation of a mercury droplet [21]. [21]

EWOD-based pumps have significant potential for microfluidic applications beyond traditional pumping. For instance, Mumcu and coworkers have introduced the concept of selectively metalized plates (SMP) that move within microfluidic channels as fluid is pumped through the system to realize reliable devices with superior efficiency and power handling capabilities [[22], [23]]. Their work has used commercial micropumps (Bartels mp-6 piezo pumps) [23], [24]. Applications include a mm-wave recongfigurable bandpass filter[24] and a [24]metallic liquid monopole antenna [25]. While features of these systems can be very small with sub millimeter channels, many use bulky external pumps. PZT micropump has been investigated [24], but, it requires a cleanroom-based 3D microfabrication process which can be expensive and time-consuming, as they require specialized equipment and facilities, as well as skilled personnel to operate and maintain the equipment.

There is still a need for reliable microfluidic reconfigurable RF devices. As mentioned, the current microfluidic-based RF devices have been primarily based on mechanical micropumps. To overcome these issues, this work evaluates the potential of a low-cost EWOD-driven micro pump that can actuate a device such as an RF switch. As there is a significant gap in the understanding of the fluid mechanics model of the actuation dynamics, this paper develops an analytical fluid dynamic model of an EWOD system and compares predictions to measurements of a simple EWOD pump. The models can identify strategies to enhance the performance of future microfluidic-based RF devices.

The remainder of this paper is organized as follows. In section 2, a dynamic model of the EWOD pump is presented as a function of all geometric and fluid parameters. Experiments that validate the model were also performed, and section 3 presents the experimental setup and approach. Section 4 provides a comparison between the analytical model and experimental results. Finally, the conclusions of the work are given in section 5.

2. Analytical Modeling

Here, we develop a model of an EWOD pump that consists of a single liquid drop in a channel that is actuated by adjusting the electric potential on discrete electrodes along the length of the channel. The drop resides in a semi-circular channel (see Figure 2-b). Surrounding the drop is another fluid (air or an immiscible liquid). Figure 2-a illustrates how the advancing and receding contact angle of the drop are altered by the activation of an electrode to generate an electrowetting force. This electrowetting force propels the droplet forward and consequently induces movement of the surrounding fluid within the channel. In this figure, the electrodes are covered by a dielectric layer, and on top of the dielectric layer, there is a hydrophobic layer. The entire channel is coated with a hydrophobic material.

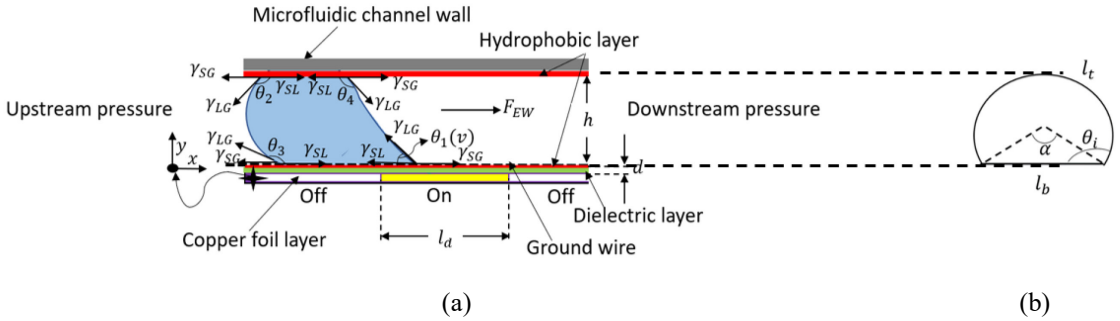

Figure 2. a) Schematic side-view of the EWOD system and the applied electrowetting force, b) Cross-section of the channel where α is equal π, indicating a half-circle arc.

The actuation uses the grounded droplet configuration. The ground potential exists inside of the drop (maintained in practice by a thin wire) and when an electrode is turned on the contact angle over that electrode will decrease significantly, yielding an electrowetting force. For the scenario considered here, electrodes exist only along the bottom surface of the channel and the semicircular walls simply provide boundaries to the droplet and surrounding fluid. For continuous actuation, a voltage is applied to electrodes ahead of the droplet as the droplet moves forward while droplets behind the droplet are grounded to provide a semi-continuous EWOD force. The width of the channel at the bottom wall is l_b (= $2h$), the radius of the semicircular channel is h and the length of each electrode along the bottom wall is l_d. Here we consider all thermophysical properties of the liquid droplet and surrounding fluid to be constant. Applying a force balance for the fluid inside the channel yields the following expression:

$$F_{Ew} - F_f = (\rho_d \forall_d + \rho_f \forall_f) \frac{d\bar{V}}{dt} \tag{2}$$

where F_{EW} is the electrowetting force, F_f is the total drag force exerted by the channel walls on the droplet and surrounding fluid. $\forall_d$ and $\forall_f$ and ρ_d and ρ_f are the volumes and densities of the droplet and surrounding fluid, respectively. $\bar{V}$ is the instantaneous average velocity of both the droplet and surrounding fluid in the channel.

The electrowetting force is determined by the energy gained from displacing the contact line. The electrowetting force can be calculated as [19]:

$$F_{Ew} = \gamma_{LG}\left[\left[l_b\left(\cos\left(\theta_1(v)\right) - \cos(\theta_3)\right) + l_t(\cos(\theta_4) - \cos(\theta_2))\right]\right. \tag{3}$$

where γ_{LG} is the surface tension coefficient between the droplet and the surrounding fluid, θ_1, and θ_3 are the advancing and receding apparent contact angles of the bottom part of the droplet over the electrode, respectively and θ_4, and θ_2 are the advancing and receding apparent contact angles of the droplet in contact with the channel. The length of the top semicircular portion of the channel is l_t and is equal to πh.

The total drag force, F_f is the viscous drag exerted on the droplet and all surrounding fluid by the channel walls. The flow is in the Stokes flow regime with the total drag force in the fully-developed laminar flow through the continuous channel [17]:

$$F_f = \frac{\bar{V} k P_w}{2D_h}\left(L_d \mu_d + L_f \mu_f\right) \tag{4}$$

where P_w is the wetted perimeter of the channel $(h(\pi + 2))$, D_h is the hydraulic diameter $(2\pi h/(\pi + 2))$, k is a geometric factor that depends on the cross-section of the channel [17], L_d and L_f are the respective lengths of the drop and the surrounding ambient fluid, and μ_d and μ_f are viscosities of the drop and the surrounding fluid. The factor k will be discussed in section 3,

Combining equations 2, 3, and 4 yields the following first-order ordinary differential equation:

$$(\rho_d \forall_d + \rho_f \forall_f) \frac{d\bar{V}}{dt} - \gamma_{LG}\left[\left[l_b\left(\cos\left(\theta_1(v)\right) - \cos(\theta_3)\right) + l_t(\cos(\theta_4) - \cos(\theta_2))\right] + \frac{\bar{V} k P_w}{2D_h}\left(L_d \mu_d + L_f \mu_f\right) = 0\right. \tag{5}$$

We solve the above nonhomogeneous first-order equation as a function of the droplet and surrounding fluid properties and channel geometric input parameters. The initial conditions are zero initial displacement of the drop and zero initial velocity. Eq. 5 allows the designer to assess the impact of different design choices on the overall performance of the electrowetting system. Model predictions are compared to experimental values in the Results section of the paper.

In addition, to measure the maximum pressure of the system in our EWOD pump device, the EWOD pressure was utilized to work against a known external pressure. Expected pressure was calculated from the Young-Laplace equation as follows:

$$\Delta p = \frac{4\varepsilon_o \varepsilon_r}{\pi h d} U^2 \tag{6}$$

where ε_r is the dielectric constant of the dielectric layer, ε_o is the permittivity of air, U is the applied voltage, d is the thickness of the dielectric layer, and h is the microchannel height.

3. Experimental Methods

In this section we describe the fabrication and assembly process of the experimental channel and electrodes. The electrowetting response, measurement of fluid properties, and the skin friction coefficient k discussed above are also described here. Lastly, the experimental setup to measure fluid velocity and maximum EWOD pump pressure is described.

3.1 Fabrication Process of the Channel and Prototype

The experimental microfluidic channel is printed using the vat polymerization method. While MEMS can offer high precision and reproducibility, it can also be more complex and expensive than other methods, such as soft lithography or 3-D printing for low volume production. In addition, gas may leak in the corners of the channel due to the small radius of curvature in the corners [26]. Vat polymerization can produce smooth channels that reduce leakage (see Figure 3-b) and is particularly valuable for applications that require quick and low-cost manufacturing. The entire channel (including electrodes) is coated with hydrophobic material. Additionally, the red line represents the ground wire held on top of the dielectric layer, ensuring that the droplet remains in contact with the ground wire throughout the entire process. As seen in Figure 3, the substrate is a print circuit board (PCB) over bare copper (SMOBC) and an Electroless Nickel Immersion Gold (ENIG) finish by Oshpark, other preparation techniques such as covering the PCB with dielectric layer and hydrophobic layer will be discussed in section 3.2. Electrode details and system assembly are illustrated in Figure 4

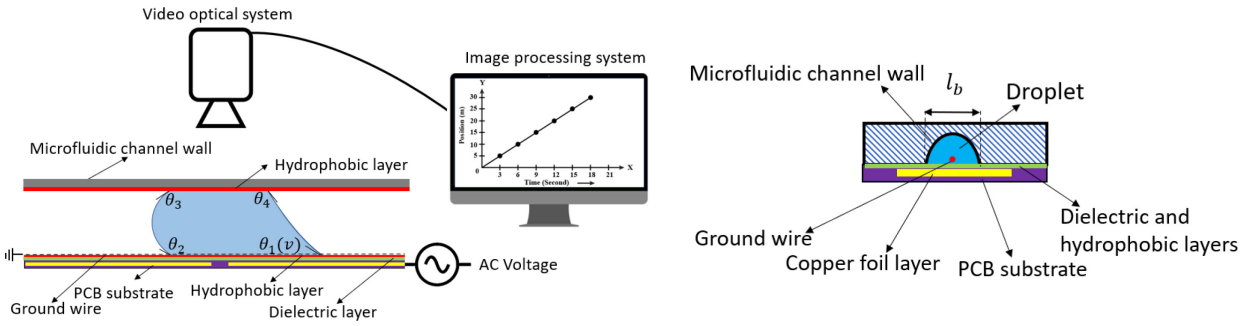

(a) (b)

Figure 3. a) Side view of channel and electrodes with optical droplet measurement technique, e) Front-view of the prototype with vat polymerization technique.

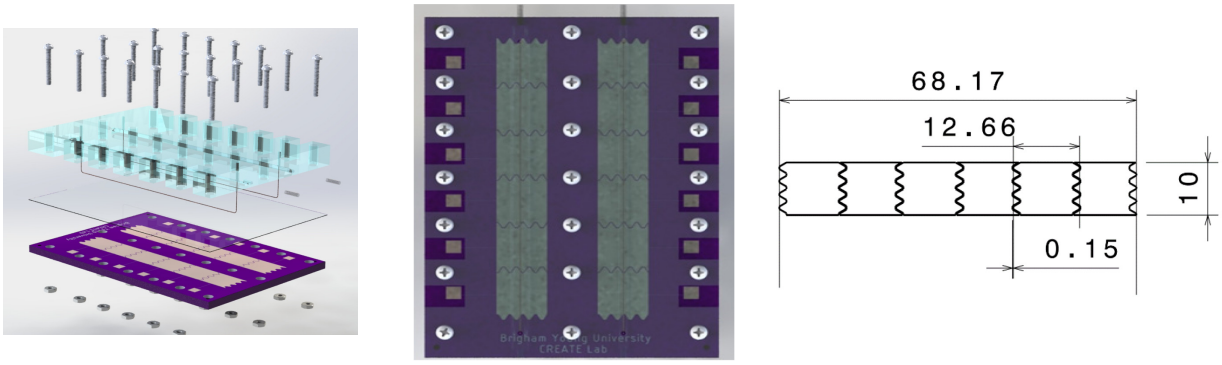

(a) (b) (c)

Figure 4. a) Exploded-view of the prototype, b) Top-view of the prototype, c) electrode pattern.

A Keyence VHX-7000 microscope at 100X magnification using the Depth Composition Mode was used to study the internal features of the 3D-printed microfluidic channel. The surface roughness was characterized with respect to printing orientation. The microscopic images reveal that the orientation of the channel during printing plays a crucial role in surface quality and in the required resin volume for supports. Figures 5-a and 5-b show that the surface quality of the channel can be improved by printing vertically rather than at an angle. By printing vertically, the 3D printed channels are smooth and uniform without need for post-processing steps, such as polishing or coating. After printing, the channel is rendered hydrophobic using multi-surface Neverwet spray. Subsequently, the channel is securely attached to the PCB using a combination of nuts and bolts as illustrated in Figure 4.

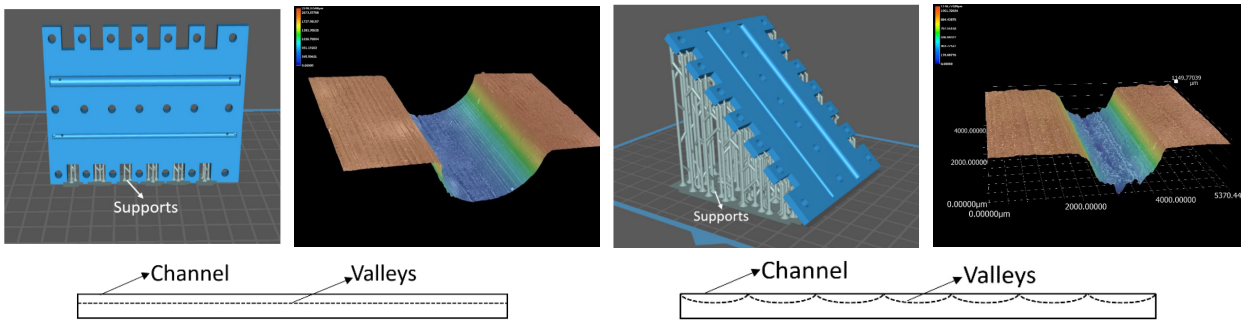

(a) (b)

Figure 5. a) A vertical printing orientation and a microscopic photo of a vertically printed channel, b) A 45° printing orientation and a microscopic photo of a non-vertically printed channel.

3.2 EWOD Preparation and Characterization

This subsection focuses on the preparation of electrodes and the application of coating layers for effective electrowetting. First, the electrodes on the PCB were coated with acrylic packing tape (100 μm) as a dielectric. Then, commercial multi-surface Neverwet spray was applied as a hydrophobic layer to minimize wetting hysteresis [27]. The base coat is responsible

for bonding with the surface and creating a rough texture, while the topcoat forms the water-repellent layer. It is known that over time the effectiveness of the NeverWet coating may diminish [27]. Thus, in all tests both the dielectric and hydrophobic layers were replaced before each test.

The electrowetting contact angle response was measured on an open electrode to estimate the electrowetting forces for the model and identify the saturation voltage. A grounded electrode setup was used with an AC voltage (frequency = 1 kHz) applied to the droplet. A droplet of the fluid of interest (3.5% salt water) with a volume of 15.7 µl was deposited on the ground electrode using an automatic syringe pump (Figure 6-a). A grounded wire is placed in the center of the droplet. The droplet shape is imaged as a function of applied voltage and the contact angle is extracted using ImageJ software. All measurements are conducted under ambient atmospheric conditions at room temperature. As shown in Figure 6-b, at zero voltage the contact angle is maximum (137.1^o). In the Young-Lippmann (YL regime), the contact angle progressively decreases at an increasing rate as the applied voltage is increased [9]. Figure 6-b shows measured drop static contact angle as a function of the applied voltage, U. The data illustrate the Young-Lipman regime at $U < 750$ V, while at $U > 750$ V the EW response saturates and the contact angle levels off at a constant value.

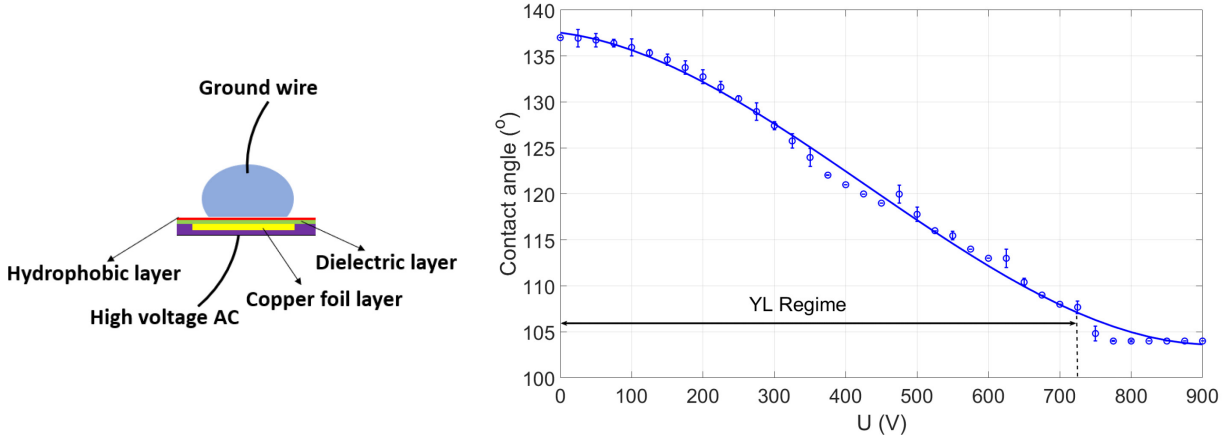

(a) (b)

Figure 6. a) Saturation voltage measurement test setup, b) Measured static droplet contact angle on the coated dielectric layer as a function of potential (EWOD curve) that shows the Young–Lippmann (YL) regime and saturation regime (specific system: ionic liquid (3.5% salt water in ambient air)).

To assess the durability of both the dielectric and hydrophobic layer, an AC voltage of 700 V (1 kHz) was applied for a duration of 5 seconds, followed by a resting period of 7 seconds. The droplet static contact angle was measured at both 750 V and 0 V and the cycle was repeated 2000 times. Figure 7 shows compares the static contact angle as a function of the number of cycles for dielectric layers with and without the hydrophobic coating. For the uncoated dielectric, the droplet contact angle changed by less than 1% up to 100 on/off cycles. In contrast, for the dielectric surface with the hydrophobic coating the contact angle varied by as much as 9.5% after 100 on/off cycles. The diminishing performance of the hydrophobic coating has a direct impact on the ability of the droplet to maintain its desired contact angle during the testing process. As a result, to ensure

accuracy both the dielectric and hydrophobic layers were replaced after no more than 10 actuations.

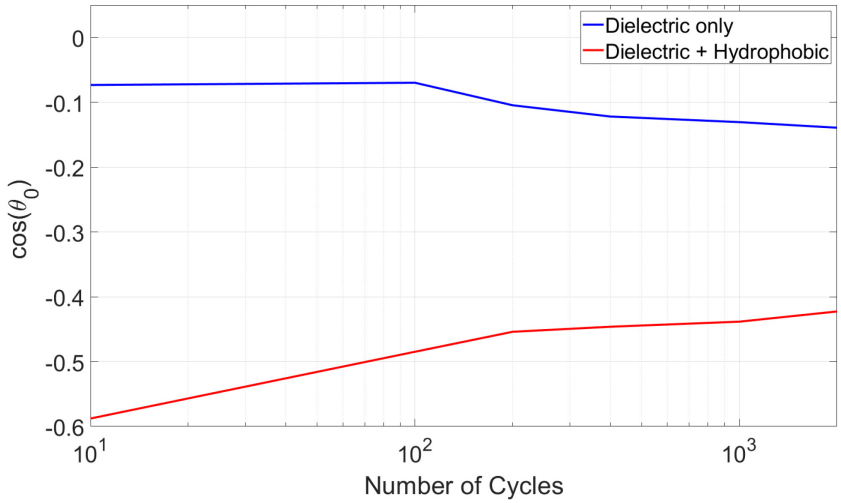

Figure 7. The static contact angle of droplet at zero voltage vs. the number of actuation cycles with/without the hydrophobic layer.

3.3 Experimental Procedures

The primary objective of the experiments is to investigate the influence of the actuation force on both the velocity of the droplet and the static pressure generated by the droplet throughout the channel. The experimental methods are described below. Together these experiments provide insights into the relationship between the applied actuation force and the resulting droplet velocity, as well as the static pressure.

3.3.1 Actuation Speed

First, the velocity of a droplet is measured as it propagates through the designed channel under zero-pressure condition by exposing the inlet and outlet of the channel to ambient conditions. This test is conducted with different electrode conditions and the time response of the droplet is compared to the model described by Equation 5.

The experiment is initiated by inserting a drop of the fluid of interest (3.5% salt water) with a volume of 7.8 µL over the ground electrode using an automatic syringe pump. The surrounding ambient fluid is air. The electrical setup is depicted in Figure 8. An AC voltage with variable amplitude from 0 to 10 V is generated at a frequency of 1 kHz using the NI USB-6343 signal generator. Subsequently, the AC voltage is amplified 100-fold. The applied voltage alters the apparent contact angle between the solid surface and the fluid to actuate the droplet. The motion of the droplet was imaged and the droplet position over time was extracted by a MATLAB Code. Each test was repeated three times, and the average velocity across the three tests is plotted. The experiment parameters are shown in Table 1.

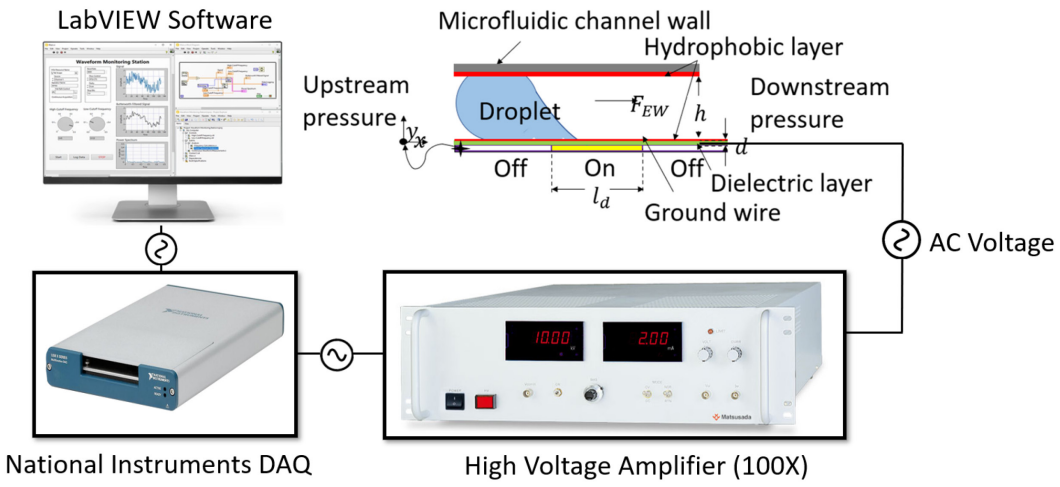

Figure 8. The electrical test setup in addition to the side view of the channel. In this setup, an AC voltage with an amplitude ranging between 0 and 10 V was generated at a frequency of 1 kHz using an NI USB-6343 signal generator and it is then amplified 100 times using a high voltage amplifier. This voltage was then applied to the PCB to actuate the droplet motion.

Table 1. Key test parameters for measuring the zero pressure electrowetting droplet response.

Fluid 1	Fluid 2	ρ_1	ρ_2	μ_1	μ_2
Water/ salt 3.5%	Air	1021 kg/m^3	1.2 kg/m^3	0.001 $^{kg}/_{m.s}$	0.000018 $^{kg}/_{m.s}$
Droplet volume	γ	L_d	L_b		
7.8 µL	43.8 mN/m	10 mm	4 mm		

3.3.2 Actuation Pressure

The second experiment is designed to measure the static pressure generated by a single electrowetting droplet. This was done using the experimental setup shown schematically in Figure 9. This setup differs from the actuation speedin that two 3-way valves have been added to the setup to connect capillary tubes to the inlet and outlet of the channel. For this experiment, silicone oil (OS-30, Dow Corning with Specific Gravity: 0.85 at 25 °C) is used as the ambient phase. A droplet of an ionic liquid with a volume of 7.8 µl is pumped into the system with a syringe pump to fully cover the ground electrode. Using the illustrated electrical system (Figure 9), a high-voltage potential is applied to the electrode just in front of the droplet, causing it to move until it completely covers the energized electrode. Next, silicone oil is slowly pumped with a programmable syringe pump at a flow rate of 5 µL/min into the system to increase the pressure until the droplet starts to move backwards. The hydrostatic pressure that exists at which the droplet begins to move back is measured by optically measuring the height difference between the inlet and outlet capillary tubes.

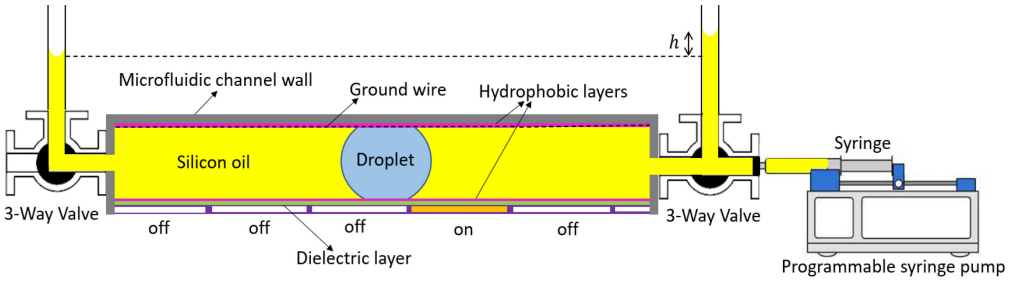

Figure 9. Schematic of the experimental setup is used to measure the maximum static pressure a single droplet can withstand. In this setup, an AC voltage with an amplitude ranging between 0 and 10 V was generated at a frequency of 1 kHz using an NI USB-6343 signal generator and it is then amplified 100 times using a high voltage amplifier.

3.4 Skin Friction Coefficient Estimation

To solve Equation (6), the skin friction coefficient k needs to be specified. This coefficient depends on channel cross-sectional shape and whether the flow is laminar and fully developed. Under fully-developed, laminar flow, this coefficient is known for many common duct shapes. However, due to the short motion and finite droplet size, fully developed flow assumptions may not be entirely valid. To evaluate the assumption of a fully developed flow for an EWOD system, numerical simulations were implemented with COMSOL™ Multiphysics software. Results from these simulations are compared with values from Table 3. Here we consider a parallel plate channel for simplicity. Figure 10 illustrates the EWOD geometry that was modeled. The fluid thermophysical values for both the surrounding fluid and the droplet are given in Table 2.

The “Phase Field” method was used for modeling the fluid–fluid interface between the droplet and ambient, which is particularly valuable in the context of the proposed multiphase flow situation, as it minimizes undesired numerical effects such as numerical diffusion or mass loss [28]. The Phase Field method produces highly accurate results with shorter computational times. This efficiency advantage becomes particularly evident when comparing it to Level Set methods [29], [30]. The simulation was initialized with all fluid initially at rest. Both the top and bottom walls were specified as no-slip boundaries. The outlet of the domain was specified as an outlet condition. Electrodes exist in the simulation along the bottom boundary. The “Ground” boundary condition is applied to all inactive electrodes and a ‘Terminal’ boundary condition (Voltage) is applied to one electrode. For all other boundaries of the model, the default ‘Zero Charge’ boundary condition is specified. When the voltage is applied in the simulation the contact angle of the drop immediately changes and motion is driven by the surface tension force acting on the drop. A mesh convergence study was conducted, leading to a maximum finite element size of 0.04 mm. An adaptive mesh algorithm was also employed, which dynamically adjusts the finite element mesh along the liquid-gas interface every 2 ms. This adaptive process employs a mesh refinement factor of 4, wherein the node distance between two nodes undergoes bisection four times, effectively increasing the mesh density in the relevant region. The bisection procedure is carried out using the longest edge method [31], incorporating error estimate algorithms as outlined in [32].

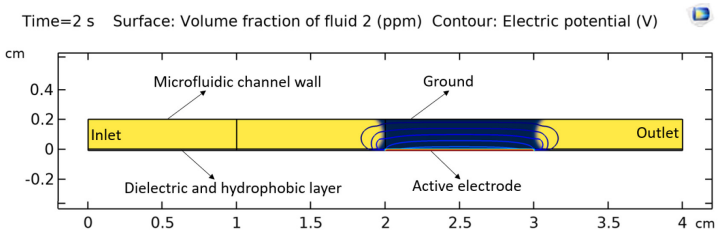

Figure 10. The FEM model of the EWOD system for a 2D parallel plate condition. . The yellow fluid is the surrounding fluid (oil) and the blue fluid is the water drop that is actuated by the electrodes.

Table 2. Key test parameters for measuring the zero pressure electrowetting droplet response .

Fluid 1	Fluid 2	ρ_1	ρ_2	μ_1	μ_2
Water	Oil	997 kg/m^3	888 kg/m^3	0.001 $^{kg}/_{m.s}$	0.011 $^{kg}/_{m.s}$
Droplet volume	L_d	L_b	V	$\Delta\theta_h$	
15.7 µL	10 mm	4 mm	700 volts	12 deg	

Figure 11 shows results from the simulation. The left axis shows the average wall shear stress on the upper and lower plates of droplet as a function of average droplet velocity. The slope of the shear stress vs. drop velocity plot, $\beta = \frac{k}{Re_{droplet\_D_H}}$, is directly related to the skin friction coefficient. Results from the simulation give different values of the skin friction coefficient depending on whether the flow is accelerating, k_{acc}, (voltage potential is on) or decelerating, k_{dec}, (voltage potential is turned off). The value for the acceleration portion of the motion is k_{acc} =19.8 and that for the decelerating portion is k_{dec} =22.3. Classical analysis for fully-develop laminar flow between parallel plates gives a constant skin friction coefficient of $k = 24$. The model predicts that the difference between simulated and fully-developed skin friction coefficients would alter peak velocity by 5.4%.

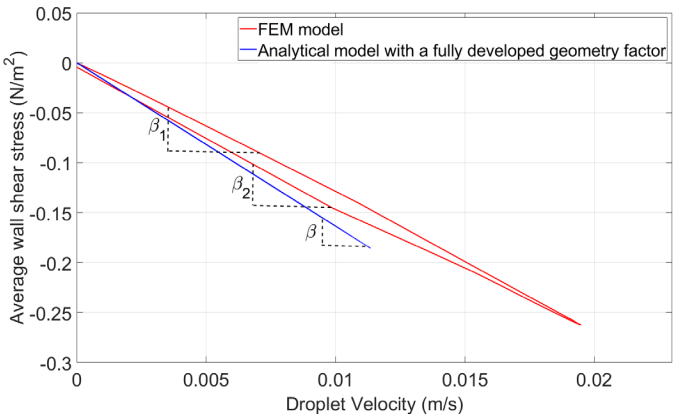

Figure 11. Average wall shear stress as a function of average droplet velocity from the FEM model.

The fully developed assumption of a constant value of k allows rapid estimation of critical design parameters of a EWOD system by using the geometry factor from fully developed model (Table 3) and solving equation (6). However, if more accuracy is desired, the designer should

utilize a full transient FEM model to estimate values of k for the accelerating and decelerating parts of the process and then solve equation (6).

Table 3. Coefficient k for different channel cross-section shapes.

	Channel shape			
	Circle	Semi-circle	Square	Parallel plate
Fully developed model [17]	$k = 16$	$k = 15.77$	$k = 14.23$	$k = 24$
Dynamic model	Different values of k can be found by the FEM model (i.e., $k_{acc} = 19.8$, and $k_{dec} = 22.3$ for the current case study)			

4. Results and Discussion

4.1 Droplet Motion Model

To verify the proposed model, first the zero-pressure condition is imposed and the velocity of the droplet through the EWOD channel is measured. The experimental parameters for the scenario are shown in Table 1. In this experiment, the droplet covers half of the electrode length. Figure 12 illustrates the direction of the driving force at key droplet positions. When voltage is initially applied (acceleration phase), the droplet is propelled forward by the electrowetting force. However, when the droplet completely covers the active electrode, the electrowetting force goes to zero, and the droplet is propelled by the inertia (glide phase). When the rear of the droplet has moved onto the activated electrode and the front of the electrode has moved to the next electrode (grounded), the electrowetting force reverses (deceleration phase), causing the droplet to stop at an equilibrium position only on the activated electrode. In this figure, the active (ON) and ground electrodes are labeled in each phase.

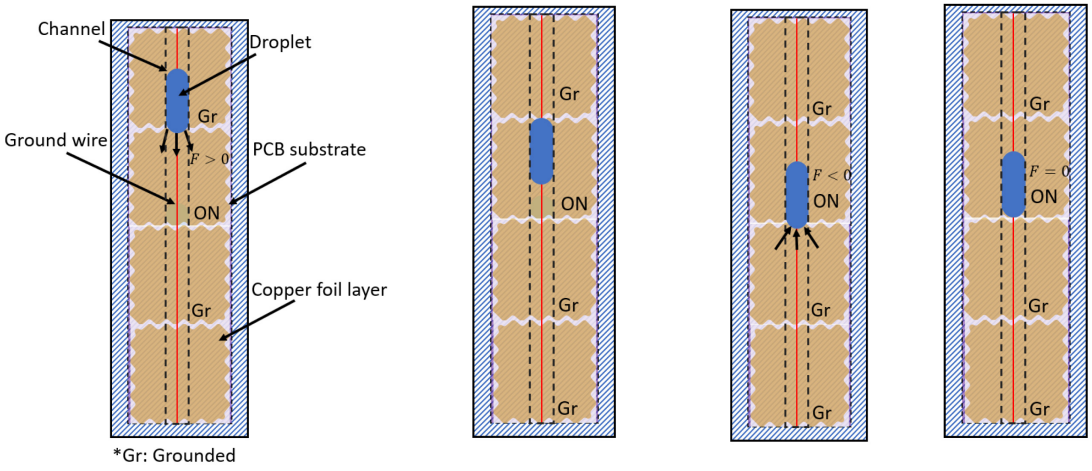

(Acceleration Phase) (Glide Phase) (Deceleration Phase) (Equilibrium Phase)

Figure 12. Illustration of the droplet motion as subsequent electrodes are activated, in this setup, when the electrode is activated (ON), the droplet is propelled forward by the electrowetting force. However, when the droplet reaches the grounded electrode, the electrowetting force reverses, causing the droplet to come to an abrupt stop at the position. In this setup, the initial conditions are zero initial displacement of the drop and zero initial velocity. The red line represents the ground wire held on top of the dielectric layer, ensuring that the droplet remains in contact with the ground wire throughout the entire process

Figure 13a,b presents the measured droplet velocity as a function of displacement and time and the analytical model predictions corresponding to actuation voltages of 650 V, 700 V, and 750 V. The position of the droplet can be used to identify the motion phase (Figure 13b). The time response (Figure 13a) facilitates comparison of acceleration rates and thus estimates of applied force. Both the experimental results and the model demonstrate that the droplet undergoes a transient acceleration while it is partially covering the energized electrode followed by a glide phase while the droplet completely covers the active electrode starting at 5.79 mm. During gliding, the viscous forces cause deceleration. However, the deceleration increases dramatically in the deceleration phase when the droplet starts to move off the energized electrode and the electrowetting force reverses direction.

In this dataset, both the model and the experiment predict that increasing voltage leads to an increase in velocity and the magnitudes of the measured and predicted peak velocity are similar with the model predicting 2.4 to 5.7% higher velocity than the measured values. Due to the low temporal resolution of the position measurements, this is within the experimental error of the velocity measurement. However, the results suggest a noteworthy average error of 14.8% in the velocity-time curve between the model's predictions and the experimental data in the acceleration, gliding, and deceleration phases, as assessed through the area under the velocity-time curve. This discrepancy can likely be attributed to the selection of the skin friction coefficient and details of the electrode shape not included in the basic model. To better understand these effects, the impact of electrode shape on the electrowetting force and the skin friction coefficient was estimated from deceleration during the glide phase.

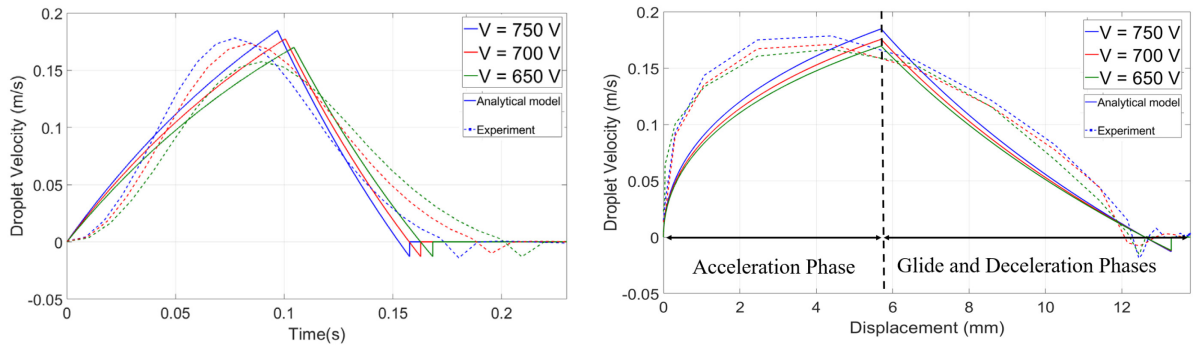

(a) (b)

Figure 13. a) Analytical model and measured droplet velocities as a function of time for three applied voltages. b) Analytical model and measured droplet velocities as a function of displacement for three applied voltages.

Details regarding the test parameters can be found in Table 1, while the test procedures are elaborated in Section 3.3.1.

4.1.1. Electrowetting Force Corrections

In the preceding subsection, the motion of the droplet was examined; however, a discrepancy between the model and experiment was observed. This disparity may be attributed to the specific details of the electrode shape. This effect is investigated in this subsection.

The basic model assumes an instantaneous force switching. This would be accurate for a straight electrode boundary with negligible gap between electrodes. However, the actual electrodes incorporate a sawtooth boundary with a 0.15 mm gap between electrodes as illustrated in Figure 5. Since EW force is proportional to the length of the droplet over the electrode, this shape will lead to a gradual ramp of the voltage with position near the electrode boundary. To understand the influence of electrode shape and the spacing between interdigitated electrodes on the system's response, we conducted simulations using a gradually ramped electrowetting force (refer to Figure 14a). Figure 14b illustrates the droplet velocity as a function of time and displacement under actuation voltages of 750 V. The figure compares data from the analytical model and experimental results for these applied voltages. The slope of the ramped force (α) was adjusted to achieve the optimal alignment between the model and experiment. The model with the idealized electrowetting force is compared to the ramped electrowetting force. As depicted in this figure, at the starting point, the velocity curve from the model exhibits a steeper slope, implying a higher electrowetting force. The ramped modelclosely alignto the experimental data in the initial acceleration phase. Thus, the discrepancy in the initial stage is likely due to the electrode shape, which is now incorporated into the model, resulting in a much improved fit of velocity over time for the first approximately 0.04s and approximately 0.87 mm, which shows the importance of the effective active length of the droplet in an electrowetting system. However, this adjustment does not alter the shape of the subsequent curve, revealing a noticeable deviation between model and experiment. This discrepancy is likely linked to the choice of the skin friction coefficient, a topic that will be further discussed in the next subsection.

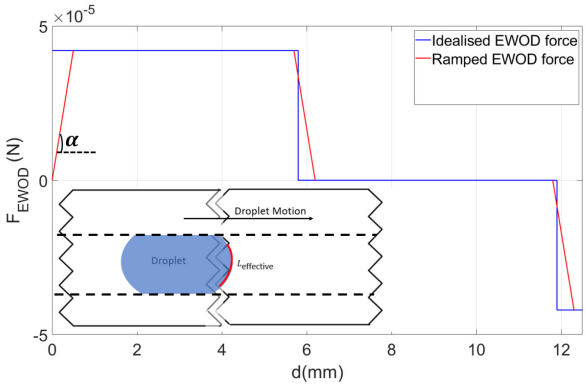

(a)

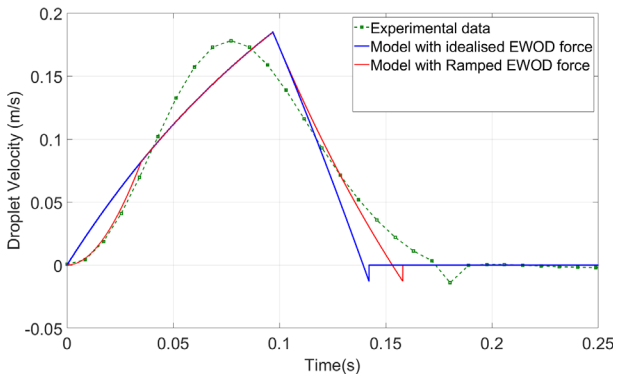

(b)

Figure 14. a) The idealized and ramped electrowetting force that have been used in the model. b) Analytical model and measured droplet velocities as a function of time details regarding the test parameters can be found in Table 1, while the test procedures are elaborated in Section 3.3.1.

4.1.2 Friction Force Corrections

Section 3.4 showed through simulation that in the 2D case, the values of the skin friction coefficient differed between the accelerating, gliding, and decelerating phase. To gain insight into the origins of disparities between the model and experimental measurements observed in Figure 14 after approximately 0.041 seconds, the experimental droplet forces can be estimated from the known droplet mass and the measured motion by taking the derivative of velocity using the following equation:

$$F_{total}(v) = F_{Ew} - F_f(v) = (\rho_d \forall_d + \rho_f \forall_f)\frac{dv}{dt} \tag{7}$$

where F_{EW} is the electrowetting force, F_f is the total drag force exerted by the channel walls on the droplet and surrounding fluid. $\forall_d$ and $\forall_f$ and ρ_d and ρ_f are the volumes and densities of the droplet and surrounding fluid, respectively.

Figure 15 compares the total force estimated from experiments using Equation 7to the model force predictions as a function of displacement. The EWOD force dominates initially, but the force declines as the friction force increases and the droplet approaches steady state velocity. When the droplet completely covers the active electrode at 5.79 mm, F_{ew} = 0 and only friction force remains. During this phase, the droplet moves forward due to inertia, but its speed gradually decreases due to the friction force.

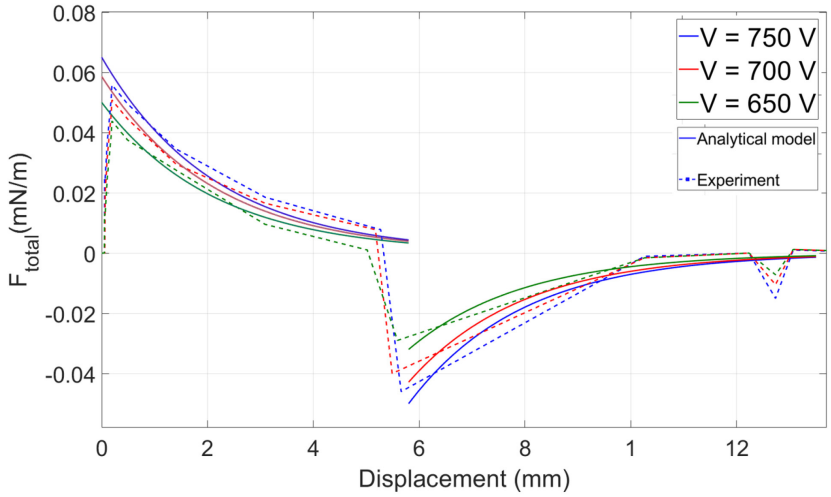

Figure 15. a) Comparison of the total force on the droplet predicted by that analytical model and estimated from the measured droplet acceleration as a function of displacement for three applied voltages. Details regarding the test parameters can be found in Table 1, while the test procedures are elaborated in Section 3.3.1.

The electrowetting force is approximately constant in each phase of motion. However, the total drag force ($F_f(v)$) is dependent on velocity. Consequently, the velocity dependence of the total force ($F_{total}(v)$) (Figure 16) can provide insights into the skin friction coefficient in equation (4). In an ideal scenario, the force-velocity curve should be a straight line, with the slope corresponding to the skin friction coefficient. However, the experiments reveal variations in skin friction coefficients during each phase, with different slopes even within a single phase. Consequently, the average of slopes will be calculated for each phase. The figure reveals that the average values for the acceleration and glide-deceleration phases are $k_1 = 17.35$ and $k_2 = 11.87$, respectively and that there is significant deviation from these values in the initial acceleration and deceleration stages. In classical analysis, assuming fully developed laminar flow in a semicircular channel yields a constant skin friction coefficient of $k = 15.77$. The assumption of a constant k value in fully developed conditions enables a swift estimation of critical design parameters for an EWOD system using the geometry factor from Table 2 and solving equation (5), but the experiments show variation. For greater accuracy, designers should employ a full 3D transient FEM model or conduct a series of experiments to estimate k values for the accelerating and decelerating phases and subsequently solve equation (6).

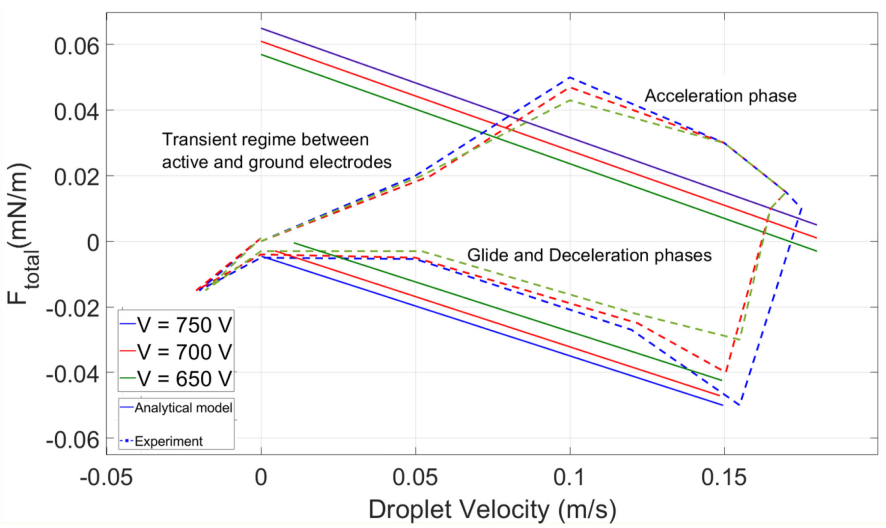

Figure 16. The total force as functions of velocity for different actuation voltages. Details regarding the test parameters can be found in Table 1, while the test procedures are elaborated in Section 3.3.1.

Additional experiments with multiple electrodes energized simultaneously provide additional insight. Figure 17a provides a visual representation of this relationship, focusing on the behavior of the droplet under an applied voltage of 750 V. Specifically, Figure 17a illustrates the experimental and model velocity profiles when three electrodes are active to extend the glide phase compared to the scenario where only one electrode is activated. Activating multiple electrodes eliminates the electrowetting reverse force.

A plot of the total force as a function of velocity (Figure 17b) offers insights into the skin friction coefficient during deceleration, as the total force during the glide phase is equivalent to the frictional force. Figure 17c illustrates the total force as a function of velocity for various voltage levels. The data points from this figure were extracted during the glide phase, where the driving electrowetting force is absent, and then re-plotted in Figure 17d. The results demonstrate a linear relationship with a skin friction coefficient of 14.23 ± 0.8 for deceleration phase. In the final step, following an understanding of the influence of electrode shape on electrowetting force and the variations in skin friction coefficient, the new skin friction coefficient, as opposed to the laminar fully developed coefficient, will be employed to estimate droplet motion. The RMSE values are 0.0012, 0.0010, and 0.00127 for 650V, 700V, and 750V, respectively. The fitting quality is superior in the early stages and in the middle of the range, particularly when the droplet is approaching a steady state. However, additional refinements are required to address the friction coefficient in the transition regions between acceleration and deceleration, where the effective friction factor deviates significantly from the steady state.

Figure 17f illustrates the behavior of the droplet under an applied voltage of 750 V, with ramped electrowetting force, incorporating data from both the model and experimental results, with $k_1 = 17.35$ and $k_2 = 14.23$. With the adjustments, the model matches experiments much better though there is still a deviation near the start of the gluide phase and the force reversal due to the change in friction coefficients at transitions.

[33]

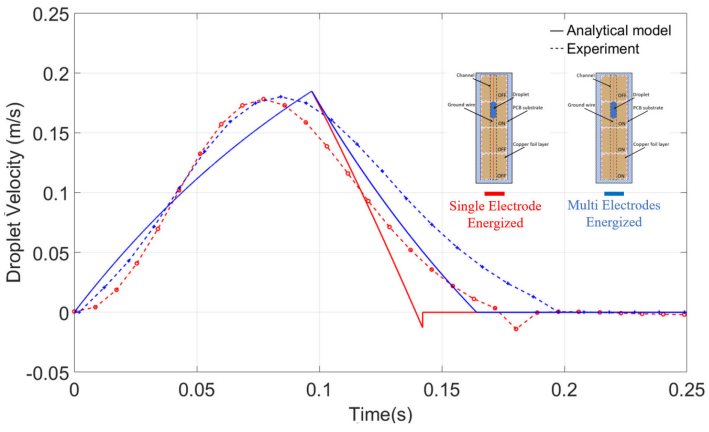

(a)

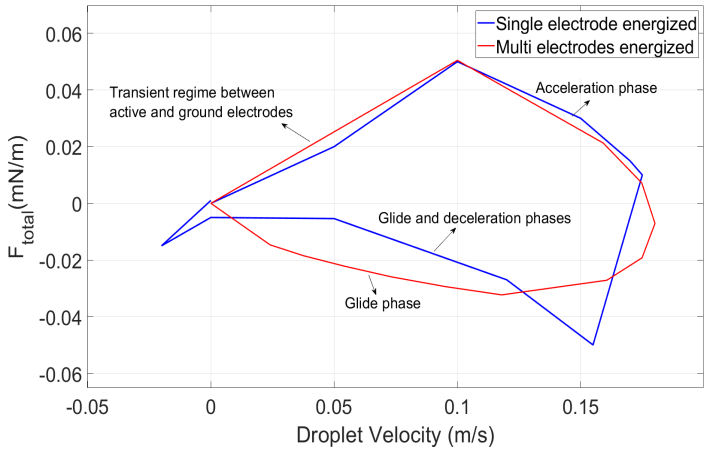

(b)

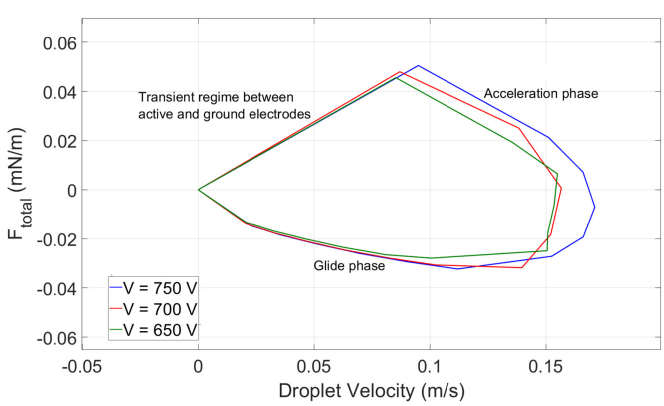

(c)

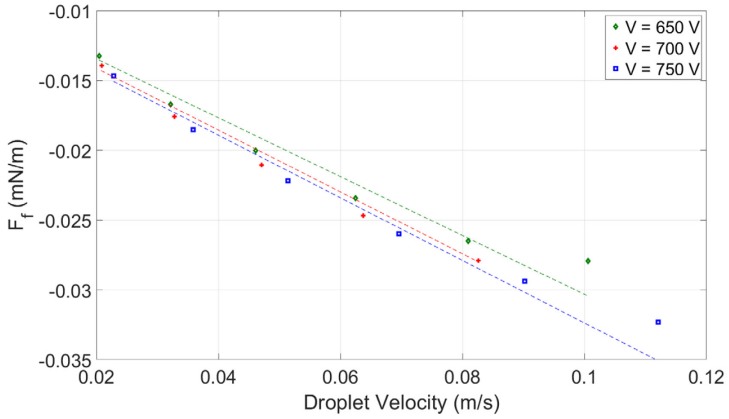

(d)

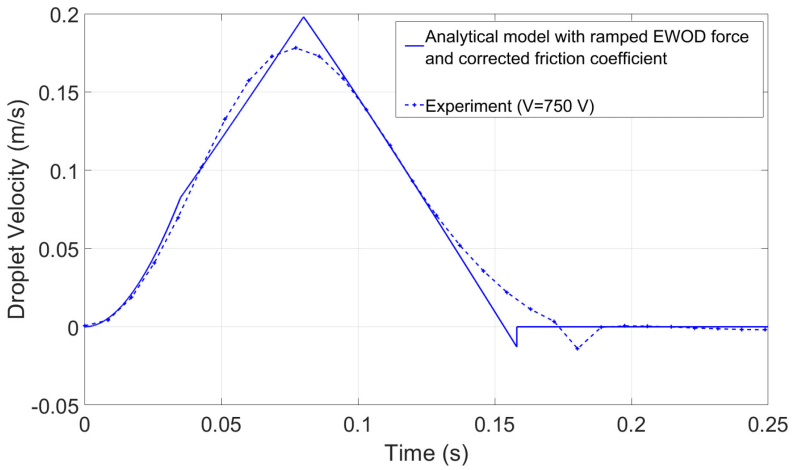

(f)

Figure 17. Analytical model and measured droplet velocities as a function of time in the presence of multiple and single active electrodes (750 V), ultimately leading to the elimination of reverse forces and an increase in the decay time, b) The total force as functions of velocity in the presence of multiple and single active electrodes (750 V), c) The total force as functions of velocity in the presence of multiple active electrodes for different applied voltage d) the friction force as function of velocity in the glide phase f) Analytical model with ramped EWOD force and corrected friction coefficient and measured droplet velocities as a function of time Details regarding the test parameters can be found in Table 1, while the test procedures are elaborated in Section 3.3.1.

4.2 Pump Pressure Measurements

In the preceding subsections, the velocity of a droplet was measured as it traversed the channel in air ambient under zero-pressure conditions, achieved by exposing the channel's inlet and outlet to the ambient environment. In this section, the focus shifts to measuring the maximum static pressure with the ambient fluid being silicon oil. Figure 18 presents the static pressure as a function of applied voltage compared to the model prediction. The measured pressure is lower than the expected value by 7.4%.

These data exhibit a poorer match compared to the previous tests conducted with air as the ambient fluid. One potential explanation for this disparity could stem from the degradation of the hydrophobic layer, possibly exacerbated by prolonged periods of applied voltage, which could accelerate electrowetting force degradation. As can be observed in Figure 7, the contact angle of the droplet in rest mode on a hydrophobic coating changed by 9.5%. This might lead to a reduction in the measured electrowetting force and/or an increase in the contact angle hysteresis. The silicone oil may also accelerate the degradation of the hydrophobic layer or oil trapped beneath the droplet may alter the electrowetting force. Improvements in the quality of fabrication and hydrophobic coating or direct measurement of the electrowetting response in silicone oil environment will result in measurements that are closer to their expected values. While degradation is a problem with this material system, this could be addressed by using a different EWOD material system that has shown reliable stable actuation [33] (ADD REF TO: https://pubs.acs.org/doi/full/10.1021/la1051468). [34] or through use of multilayer dieletrics (https://www.sciencedirect.com/science/article/pii/S0040609013004392). In addition to the surface and coating material, Diebold, et al., showed that low loss RF conductive fluids such as room temperature liquid metals (i.e. Hg, EGaIn, Galinstan) can improve the performance of a RF EWOD system [35].

If desired, the static pressure can be enhanced by arranging droplets in series, as illustrated in Figure 19. The pressure should increase linearly with the number of droplets in series.

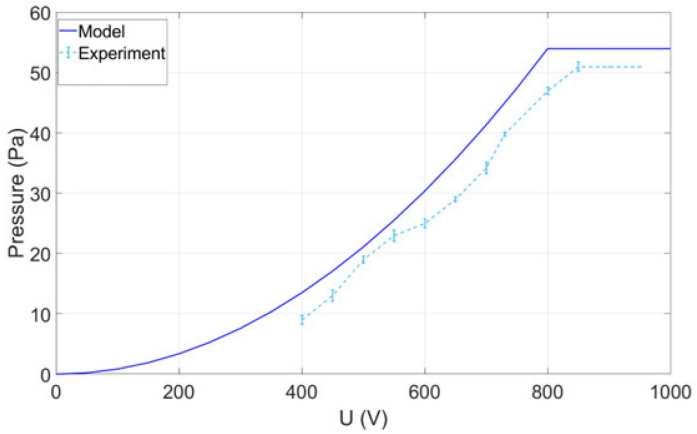

Figure 18. The model and measured droplet pressure as a function of applied voltage.

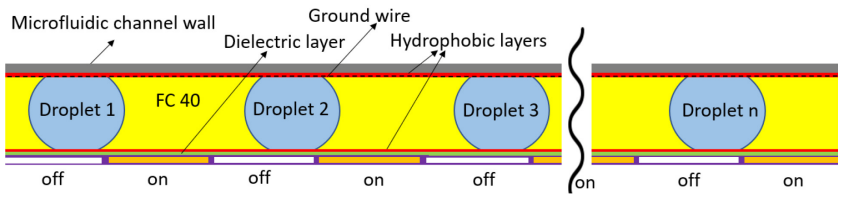

Figure 19. The schematic figure of EWOD system with droplets in series.

4.3 Other Design Considerations

The model can be utilized to evaluate the performance of the proposed EWOD semicontinuous pump and identify conditions that could enhance its competitiveness as an actuation system. In this case study, we employed a 3D variant of the model (see figure 20). The simulation parameters were derived from Table 1, and the electrical setup closely resembled that presented in Figure 8. In Figure 20a, the maximum droplet velocity as a function of channel height was plotted to examine the impact of varying the channel height h. the electrowetting force is constant with the channel height, it increases the inertial force by enlarging the volume of the droplet. For instance, in this case study (the simulation parameters are taken from Table 1, and the electrical configuration is similar to Figure 8), the electrowetting force remains dominant until the channel height, h, reaches 0.71 mm. Furthermore, Figure 20b demonstrates the relationship between the maximum droplet velocity and channel length. Increasing the length of the droplet reduces droplet velocity since it increases the inertial force and the friction area.

Using low-viscosity fluids can decrease the friction force which will increase the droplet velocity. One possible way to achieve this is by increasing the working temperature. However, the result reveals that the droplet velocity will increase only by 11.5% by increasing the working temperature 30^{o}C. In addition, this method may damage the dielectric layer and hydrophobic coating. It is essential for designers to carefully consider the trade-offs and potential benefits of different approaches and evaluate their feasibility and effectiveness using the proposed analytical model.

Overall, by using the model, designers can assess the impact of various design parameters, such as channel width, length, and height, on the system's overall performance. They can also examine the effects of fluid properties, such as density and viscosity, on the electrowetting force, friction force, and inertia force to identify the most promising fluid options for their specific application. While this model has been applied to the transient analysis of a single droplet step, this could be readily extended to study other factors such as actuating a series of electrodes in sequence for continuous motion.

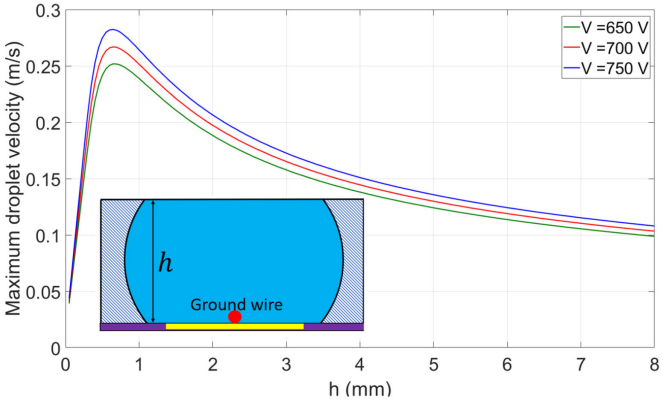

(a)

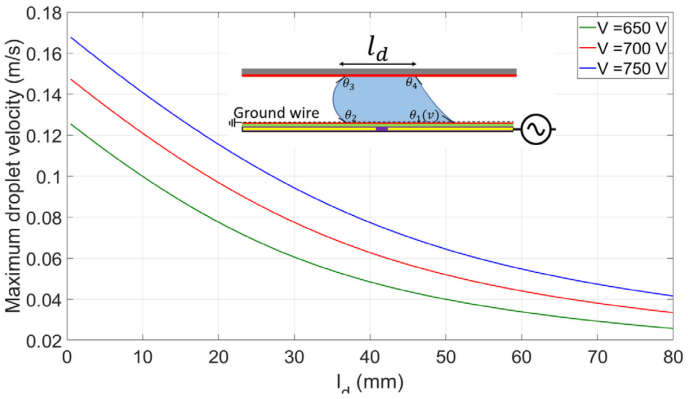

(b)

Figure 20. Simulation result of maximum droplet velocity as a function of a) channel height, b) length of the droplet, while other parameters are kept constant; the simulation parameters are taken from Table 2, and the electrical configuration is similar to Figure 10.

The main advantage of the semicontinuous EWOD pump over previous micromechanical pumps lies in its simple 2D manufacturing process, which allows for embedding with metalized plates and RF circuit boards, making it compact, portable, and low-cost. Additionally, the EW pump does not include any moving mechanical components, which may increase the system's reliability in harsh environments. Further investigations are necessary to integrate the proposed semicontinuous pump into applications such as microfluidic reconfigurable RF devices and evaluate resulting performance.

5. [Conclusion and Future Work

This paper presents a design methodology for an EWOD semicontinuous micropump which may overcome current technology issues in microscale actuation applications such as microfluidic reconfigurable radio frequency devices. The analytical model developed herein establishes a relationship between displacement and velocity within the EWOD-actuated system, taking into account variations in input voltage, and has been validated through experimental data. Our findings demonstrate a low error rate, with a deviation of less than 6% between the measured and modeled maximum velocities, and a maximum error of 7.4% observed for static pressure.

The study highlights the significant impact of electrode configuration, such as the use of interdigitated electrodes, in inducing a gradual and smooth motion during the transition between active and grounded electrodesThe friction force in these droplets is shown to vary with direction and to change significantly during changes of direction. These effects must be accounted for if greater model accuracy is needed.

The proposed analytical model offers a valuable tool for understanding the complex interplay between the electrowetting force, friction force, and inertia force in electrowetting systems. By leveraging this model, designers can effectively evaluate different design options and identify the limits of potential actuation performance for fluids in channels. Specifically, the model allows designers to explore the trade-offs between channel dimensions, fluid properties, and working conditions to optimize the performance of the system.

For future work, the proposed semicontinuous EWOD micropump can integrate with an RF device. Increasing the applied voltage to achieve higher pressures has limitations, such as contact angle saturation, electrolysis, and dielectric breakdown. Adding droplets may provide a way to achieve higher pressures without encountering some of the limitations associated with higher voltages. However, it also introduces other challenges, such as issues related to droplet stability, droplet size control, and the need to manage multiple droplets. This model will facilitate assessment of the trade-offs and potential benefits of different approaches.

ACKNOWLEDGMENTS

The authors wish to thank Dr. Gokhan Mumcu for providing additional information on the experimental setup at the Department of Electrical Engineering at the University of South Florida. The work is supported in part by the National Science Foundation through Grant No. 1920953.

REFERENCE

[1] Y. Song, D. Cheng, and L. Zhao, *Microfluidics: fundamentals, devices, and applications*. 2018. Accessed: Apr. 23, 2023. [Online]. Available: https://books.google.com/books?hl=en&lr=&id=dnNVDwAAQBAJ&oi=fnd&pg=PR13&dq=Microfluidics:+fundamentals,+devices,+and+applications.+John+Wiley+%26+Sons.&ots=fwbZR6tJvd&sig=VS40VU7hPqPdZufojXR4v5rhqIo

[2] V. Narayanamurthy *et al.*, "Advances in passively driven microfluidics and lab-on-chip devices: A comprehensive literature review and patent analysis," *RSC Adv*, vol. 10, no. 20, pp. 11652–11680, Mar. 2020, doi: 10.1039/d0ra00263a.

[3] C. W. Nelson, C. M. Lynch, and N. B. Crane, "Continuous electrowetting via electrochemical diodes," *Lab Chip*, vol. 11, no. 13, pp. 2149–2152, Jul. 2011, doi: 10.1039/c1lc20196d.

[4] F. Mugele and J. Heikenfeld, *Electrowetting : fundamental principles and practical applications*.

[5] F. Mugele and J. C. Baret, "Electrowetting: From basics to applications," *Journal of Physics Condensed Matter*, vol. 17, no. 28. IOP Publishing, p. R705, Jul. 20, 2005. doi: 10.1088/0953-8984/17/28/R01.

[6] Q. Ni, D. E. Capecci, and N. B. Crane, "Open-loop electrowetting actuation with micro-stepping," *Sens Actuators A Phys*, vol. 247, pp. 579–586, Aug. 2016, doi: 10.1016/j.sna.2016.06.034.

[7] Q. Ni and N. B. Crane, "Electrowetting Effect: Theory, Modeling, and Applications," in *Wiley Encyclopedia of Electrical and Electronics Engineering*, Hoboken, NJ, USA: John Wiley & Sons, Inc., 2015, pp. 1–14. doi: 10.1002/047134608X.W8290.

[8] Q. Ni, "Droplet-based Mechanical Actuator Utilizing Electrowetting Effect," *USF Tampa Graduate Theses and Dissertations*, Jun. 2016, Accessed: Oct. 24, 2022. [Online]. Available: https://digitalcommons.usf.edu/etd/6337

[9] Q. Ni, D. E. Capecci, and N. B. Crane, "Electrowetting force and velocity dependence on fluid surface energy," *Microfluid Nanofluidics*, vol. 19, no. 1, pp. 181–189, Jul. 2015, doi: 10.1007/s10404-015-1563-7.

[10] K. Suzuki, H. Homma, T. Murayama, S. Fukuda, H. Takanobu, and H. Miura, "Electrowetting-Based Actuation of Liquid Droplets for Micro Transportation Systems*," *Journal of Advanced Mechanical Design*, vol. 4, no. 1, pp. 365–372, 2010, doi: 10.1299/jamdsm.4.365.

[11] M. Abdelgawad, M. W. L. Watson, and A. R. Wheeler, “Hybrid microfluidics: A digital-to-channel interface for in-line sample processing and chemical separations,” *Lab Chip*, vol. 9, no. 8, pp. 1046–1051, 2009, doi: 10.1039/b820682a.

[12] C. Zhang and D. Xing, “Single-molecule DNA amplification and analysis using microfluidics,” *Chem Rev*, vol. 110, no. 8, pp. 4910–4947, Aug. 2010, doi: 10.1021/cr900081z.

[13] Z. Hua *et al.*, “Multiplexed real-time polymerase chain reaction on a digital microfluidic platform,” *Anal Chem*, vol. 82, no. 6, pp. 2310–2316, Mar. 2010, doi: 10.1021/ac902510u.

[14] W. Wang, Q. Wang, K. Zhang, X. Wang, A. Riaud, and J. Zhou, “On-demand contact line pinning during droplet evaporation,” *Sens Actuators B Chem*, vol. 312, Jun. 2020, doi: 10.1016/j.snb.2020.127983.

[15] K. Suzuki, H. Homma, T. Murayama, S. Fukuda, H. Takanobu, and H. Miura, “Electrowetting-Based Actuation of Liquid Droplets for Micro Transportation Systems*,” *Journal of Advanced Mechanical Design*, vol. 4, no. 1, pp. 365–372, 2010, doi: 10.1299/jamdsm.4.365.

[16] J. Peng *et al.*, “All-in-One digital microfluidics pipeline for proteomic sample preparation and analysis,” *Chem Sci*, Feb. 2023, doi: 10.1039/d3sc00560g.

[17] S. Morishita, M. Kubota, Y. M.-2012 I. 25th International, and undefined 2012, “Integration of EWOD pumping device in deep microfluidic channels using a three-dimensional shadowmask,” *ieeexplore.ieee.org*, Accessed: Apr. 23, 2023. [Online]. Available: https://ieeexplore.ieee.org/abstract/document/6170250/

[18] S. Yang, C. L.-T. 2009-2009 International, and undefined 2009, “An Electrolysis-bubble-actuated micropump using electrowetting on dielectric (EWOD) for 1XN micro-sample switches,” *ieeexplore.ieee.org*, Accessed: Apr. 23, 2023. [Online]. Available: https://ieeexplore.ieee.org/abstract/document/5285659/

[19] H. Phi, S. Bohm, E. Runge, … S. S.-M., and undefined 2021, “Wafer-level fabrication of an EWOD-driven micropump,” *ieeexplore.ieee.org*, Accessed: Apr. 23, 2023. [Online]. Available: https://ieeexplore.ieee.org/abstract/document/9698369/

[20] J. Kedzierski, S. Berry, and B. Abedian, “New generation of digital microfluidic devices,” *Journal of Microelectromechanical Systems*, vol. 18, no. 4, pp. 845–851, 2009, doi: 10.1109/JMEMS.2009.2023845.

[21] K. S. Yun, I. J. Cho, J. U. Bu, C. J. Kim, and E. Yoon, “A surface-tension driven micropump for low-voltage and low-power operations,” *Journal of Microelectromechanical Systems*, vol. 11, no. 5, pp. 454–461, Oct. 2002, doi: 10.1109/JMEMS.2002.803286.

[22] A. Qaroot and G. Mumcu, “Microfluidically Reconfigurable Reflection Phase Shifter,” *IEEE Microwave and Wireless Components Letters*, vol. 28, no. 8, pp. 684–686, Aug. 2018, doi: 10.1109/LMWC.2018.2847046.

[23] T. Palomo and G. Mumcu, “Microfluidically Reconfigurable Microstrip Line Combline Filters with Wide Frequency Tuning Capabilities,” *IEEE Trans Microw Theory Tech*, vol. 65, no. 10, pp. 3561–3568, Oct. 2017, doi: 10.1109/TMTT.2017.2730181.

[24] E. Gonzalez-Carvajal and G. Mumcu, “Frequency and Bandwidth Tunable mm-Wave Hairpin Bandpass Filters Using Microfluidic Reconfiguration with Integrated Actuation,” *IEEE Trans Microw Theory Tech*, vol. 68, no. 9, pp. 3756–3768, Sep. 2020, doi: 10.1109/TMTT.2020.3006869.

[25] E. Park, M. Lee, and S. Lim, “Switchable Bandpass/Bandstop Filter Using Liquid Metal Alloy as Fluidic Switch,” *Sensors*, vol. 19, no. 5, p. 1081, Mar. 2019, doi: 10.3390/s19051081.

[26] P. Pal, K. Sato, M. Shikida, and M. A. Gosálvez, “Study of corner compensating structures and fabrication of various shapes of MEMS structures in pure and surfactant added TMAH,” *Sens Actuators A Phys*, vol. 154, no. 2, pp. 192–203, Sep. 2009, doi: 10.1016/j.sna.2008.09.002.

[27] R. Gupta, V. Vaikuntanathan, and D. Sivakumar, “Superhydrophobic qualities of an aluminum surface coated with hydrophobic solution NeverWet,” *Colloids Surf A Physicochem Eng Asp*, vol. 500, pp. 45–53, Jul. 2016, doi: 10.1016/j.colsurfa.2016.04.017.

[28] X. Cai, H. Marschall, … M. W.-C. E., and undefined 2015, “Numerical Simulation of Wetting Phenomena with a Phase-Field Method Using OpenFOAM â,” *Wiley Online Library*, vol. 38, no. 11, pp. 1985–1992, Nov. 2015, doi: 10.1002/ceat.201500089.

[29] M. Nahar, … G. B.-P. of the, and undefined 2015, “Numerical modeling of 3D electrowetting droplet actuation and cooling of a hotspot,” *dvdachetez.com*, Accessed: May 09, 2023. [Online]. Available: https://www.dvdachetez.com/paper/download/257441/nahar_paper.pdf

[30] H. Amiri, A. H.-I. J. of M. Flow, and undefined 2013, “Evaluation of level set and phase field methods in modeling two phase flow with viscosity contrast through dual-permeability porous medium,” *Elsevier*, Accessed: May 09, 2023. [Online]. Available: https://www.sciencedirect.com/science/article/pii/S0301932212001796

[31] M. C. Rivara, “Algorithms for refining triangular grids suitable for adaptive and multigrid techniques,” *Int J Numer Methods Eng*, vol. 20, no. 4, pp. 745–756, 1984, doi: 10.1002/nme.1620200412.

[32] I. Babuvška and W. C. Rheinboldt, “Error Estimates for Adaptive Finite Element Computations,” *SIAM J Numer Anal*, vol. 15, no. 4, pp. 736–754, Aug. 1978, doi: 10.1137/0715049.

[33] M. Khodayari, J. Carballo, and N. B. Crane, “A material system for reliable low voltage anodic electrowetting,” *Mater Lett*, vol. 69, pp. 96–99, Feb. 2012, doi: 10.1016/j.matlet.2011.11.060.

[34] Q. Ni, D. E. Capecci, M. Schlafly, and N. B. Crane, “Robust bidirectional continuous electrowetting based on metal–semiconductor (M–S) diodes,” *Microfluid Nanofluidics*, vol. 20, no. 8, pp. 1–9, Aug. 2016, doi: 10.1007/s10404-016-1788-0.

[35] A. V. Diebold *et al.*, “Electrowetting-actuated liquid metal for RF applications,” *Journal of Micromechanics and Microengineering*, vol. 27, no. 2, p. 025010, Feb. 2017, doi: 10.1088/1361-6439/aa556a.